JOURNAL OF CATALYSIS 135, 367–385 (1992)

Structures and Catalytic Activity of Pt–Mo Bimetallic Ensembles Derived from a New Planar $[PtMo_6O_{24}]^{8-}$ Heteropolyanion Supported on Al_2O_3 and SiO_2

I. Characterization of the Supported $[PtMo_6]$ Catalysts

T. LIU, K. ASAKURA, U. LEE,* Y. MATSUI,† AND Y. IWASAWA[1]

*Department of Chemistry, Faculty of Science, University of Tokyo, Hongo, Bunkyo-ku, Tokyo 113, Japan; *Department of Chemistry, National Fisheries University of Pusan, Nam-ku, Pusan 608-737, Korea; and †National Institute for Research in Inorganic Materials, Namiki 1-1, Tsukuba, Ibaraki 305, Japan*

Received April 16, 1991; revised January 22, 1992

Pt–Mo bimetallic ensembles active for ethene hydrogenation and ethane hydrogenolysis were prepared on silica and alumina using a new Anderson-type plane $[PtMo_6O_{24}]^{8-}$ heteropolyanion as a precursor. The structures of the supported bimetallic ensembles were determined by H_2-chemisorption, TEM (transmission electron microscopy), analytical TEM, XRD (X-ray diffraction), EXAFS (extended X-ray absorption fine structure), and XANES (X-ray absorption near edge structure). The heteropolyanion framework was maintained when it was supported on silica, but was broken when on alumina. After reduction at 773–823 K, dispersed particles with an "eggshell" structure (3.0 ± 0.5 nm) were formed on silica, where a small platinum cluster (ca. 1.0 nm) located in the center was covered with partially oxidized Mo-oxide layers. On alumina bimetallic clusters of 2.0 ± 0.5 nm were formed, and part of the molybdenum was involved in the bimetallic particle in zero valency and the remaining molybdenum atoms were dispersed in low valence states on the Al_2O_3 surface.

INTRODUCTION

Bimetallic systems have been demonstrated to modify the catalysis of each component and to create new catalytic properties. However, bimetallic active sites on oxide supports prepared by a conventional coimpregnation method are often heterogeneous and ill-defined, and hence it is difficult to find factors important for the genesis of catalysis to develop new and efficient catalytic systems. The use of bimetallic clusters as precursors provides a potential preparation of homogeneous and well-dispersed bimetallic ensembles on supports (*1, 2*).

Pt–Mo bimetallic catalysts have been reported to show higher activities for hydrogenolysis reaction than Pt or Mo monometallic catalysts (*3*). Pt–Mo bimetallic catalysts have been prepared in various ways, such as the interaction of organic complexes of platinum with presupported molybdates (*4–9*), the deposition of $Mo(CO)_6$ on presupported platinum particles (*3, 10, 11*), and a usual coimpregnation method (*12*). In the present study, we used an Anderson-type heteropolyanion $[PtMo_6O_{24}]^{8-}$ with a plane structure as a bimetallic ensemble precursor.

The hexamolybdoplatinate(IV) ion, $[PtMo_6O_{24}]^{8-}$, was recently synthesized and determined by X-ray diffraction to have an Anderson structure (*13*). The polyanion $[PtMo_6O_{24}]^{8-}$ structure, shown in Fig. 1, has a hexagonal plane structure composed of a central Pt(IV) ion surrounded by six octahedral molybdates (MoO_6). Each MoO_6 shares an edge with each of its two neighboring MoO_6 and another edge with the PtO_6 octahedron. Such a plane structure has the ad-

[1] To whom correspondence should be addressed.

0021-9517/92 $5.00

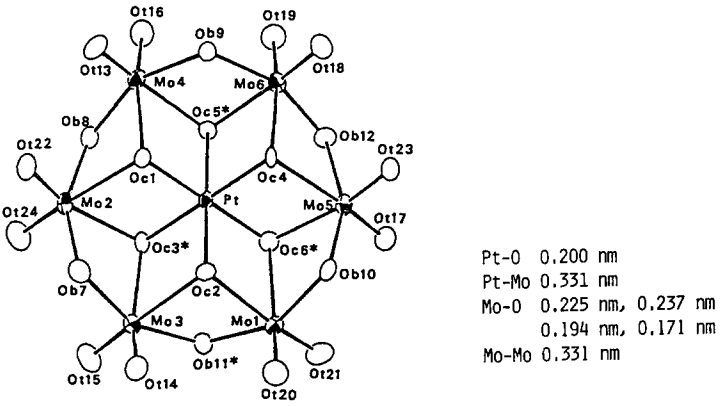

FIG. 1. Framework structure of the $[PtMo_6O_{24}]^{8-}$ heteropolyanion. (* protonated oxygen atom.)

vantage of contact with the support surface structure well.

We found that the $[PtMo_6]$ catalyst derived from $[PtMo_6O_{24}]^{8-}$ supported on Al_2O_3 showed remarkably high activity for ethane hydrogenolysis and ethene hydrogenation (*14*). On the other hand, no activity was observed with the $[PtMo_6]$ particles on SiO_2. In this report we examine the structures of the $[PtMo_6]$ bimetallic catalysts.

EXPERIMENTAL

Preparation of Catalysts

Silica, Aerosil 200 (200 m^2/g), and alumina, Alon C (100 m^2/g), obtained from Nippon Aerosil Corp., were used as supports. Chloroplatinic acid and ammonium heptamolybdate were purchased from Nakarai, Inc. and Wako Pure Chemical Industries, respectively. The planar hexamolybdoplatinate (IV) was precipitated from an aqueous solution of $(NH_4)_2[Pt(OH)_6]$ and $(NH_4)_6[Mo_7O_{24}]$ with a ratio of 1 : 6 at pH 6.4 in a way similar to that previously reported (*13*).

The supported $[PtMo_6]$ bimetallic catalysts were prepared by impregnating Al_2O_3 or SiO_2 with the aqueous solution of the $[PtMo_6O_{24}]^{8-}$ polyanion. For comparison, the Pt–Mo bimetallic catalyst was also prepared by a traditional coimpregnation method using an aqueous solution of a mixture of chloroplatinic acid and ammonium heptamolybdate. Pt/Al_2O_3 and Mo/Al_2O_3 catalysts were obtained by impregnation of the Al_2O_3 with an aqueous solution of chloroplatinic acid or ammonium heptamolybdate, respectively. The metal loadings were always 1 wt% of Pt and/or 3 wt% of Mo. After impregnation, the samples were dried at 393 K for 12 h and reduced with hydrogen (13.3 kPa) at given temperatures *in situ* before characterization and catalytic reactions. The Pt–Mo bimetallic catalysts prepared by use of $[PtMo_6O_{24}]^{8-}$ and by the coimpregnation method are denoted as $[PtMo_6]$/support and Pt–Mo/support, respectively. The reduction temperature is noted by the numeral after the catalyst; thus $[PtMo_6]/Al_2O_3$–773R indicates that $[PtMo_6]/Al_2O_3$ reduced at 773 K.

Characterization of Catalysts

The amount of hydrogen adsorption was volumetrically measured at 298 K and 13.3 kPa of hydrogen by using 2 g of catalyst reduced at various reduction temperatures and evacuated at the same temperatures. It took 1 h to reach equilibrium for chemisorption.

X-ray diffraction (XRD) measurements were obtained with a Rigaku diffractometer employing $CuK\alpha_1$ radiation (λ = 0.15405 nm). The X-ray tube was operated at a volt-

age of 35 kV and a tube current of 15 mA. Transmission electron microscope measurements for determination of particle sizes were taken by a JEM 2000EX (JEOL) operated at 200 kV. After reduction or reaction, the samples were stored under vacuum until measurements were made. Samples were dispersed in tetrachloromethane by supersonic wave and put on Cu grids. An analytical microscope (JEM 2010) in a high-resolution mode (10 nm area) was used to measure the composition of Pt and Mo in bimetallic particles.

X-ray absorption spectra at the Pt L_3 and Mo K absorption edges were measured at the BL-10B station of the Photon Factory in the National Laboratory for High-Energy Physics (KEK-PF) with a positron energy of 2.5 GeV and a maximum storage ring current of 350 mA. X-ray absorption data were collected in a transmission mode using ionization chambers filled with N_2 for the Pt L_3-edge or Ar for the Mo K-edge. A Si (311) channel-cut crystal monochromator was used since it has no second-order harmonics. Energy resolution was estimated to be 2.5 eV at the Pt L_3-edge and 8 eV at the Mo K-edge from the white line in the Br_2 K-edge (*15*). The samples were treated in a closed circulating system and transferred to an aluminum cell equipped with Kapton windows for X-ray absorption measurements without contacting air. The cell was 4 mm thick for the Mo K-edge and 6 mm thick for the Pt L-edges to allow enough edge height and a total absorbance of $\mu x \leqq 3$. Disturbance from the higher harmonics to the Pt L_3-edge EXAFS was negligible because of the low intensity of the third-order higher harmonics of the synchrotron radiation and the low detection efficiency of N_2 gas in ionization chambers. The EXAFS measurements were performed at 293 and 80 K. Platinum and molybdenum foils were used for energy calibration. Data were analyzed by the EXAFS analysis program "EXAFS2N" (*16*). The analysis involves preedge extrapolation, background removal by a cubic spline method to extract EXAFS data, and Fourier transformation using a Hanning window function with one-tenth of the FT range. The typical ranges of Fourier transformation from the k space to the r space are 30–150 nm^{-1} for the Pt L_3-edge and 30–130 nm^{-1} for the Mo K-edge. The inverse Fourier transformation to the k space and the curve fitting are carried out to obtain detailed structural information. Empirical parameters calculated from Pt foil, $[PtMo_6O_{24}]^{8-}$, Mo foil, and K_2MoO_4 were used as references to analyze the EXAFS spectra. Phase shift function and backscattering amplitude of $[PtMo_6O_{24}]^{8-}$ were used for analyzing Mo–Pt bonding. In order to compensate for differences in chemical state the threshold absorption energy (ΔE_0) is adjusted in the analysis of the Pt–Mo pair.

RESULTS AND DISCUSSION

H_2-Chemisorption and TEM

The H_2 uptake per Pt atom of various samples as a function of reduction temperature is shown in Fig. 2. Nearly 100% H_2 chemisorption is observed with the Pt/Al_2O_3 catalyst reduced at 473–673 K. The H_2 uptake for $[PtMo_6]/Al_2O_3$ is 45–60%, which is smaller than that for Pt/Al_2O_3 but larger than that for $Pt–Mo/Al_2O_3$. The $[PtMo_6]/SiO_2$ shows much smaller amounts of H_2 chemisorption than the other samples.

The metal particle sizes of bimetallic samples were estimated by TEM. Figure 3 shows the TEM photographs (magnification of 250,000) of $[PtMo_6]/Al_2O_3$–823R, $[PtMo_6]/SiO_2$–773R, and $Pt–Mo/Al_2O_3$–773R. Figure 4 shows the particle size distribution obtained by counting at least 10,000 particles. Particles with average size of 2.0 nm are observed with $[PtMo_6]/SiO_2$ reduced at 473 K, indicating the aggregation of $[PtMo_6O_{24}]^{8-}$ on SiO_2 surface. Upon reduction at 773 K the particle enlarges to 3.0 ± 0.5 nm. On the other hand, no Pt particles are observed for $[PtMo_6]/Al_2O_3$ reduced at temperatures below 473 K. The $[PtMo_6]/Al_2O_3$ sample reduced at 773 K shows a particle size of 2.0 ± 0.5 nm with a narrow distribution. The coimpregnated catalyst shows a broad distribution. The

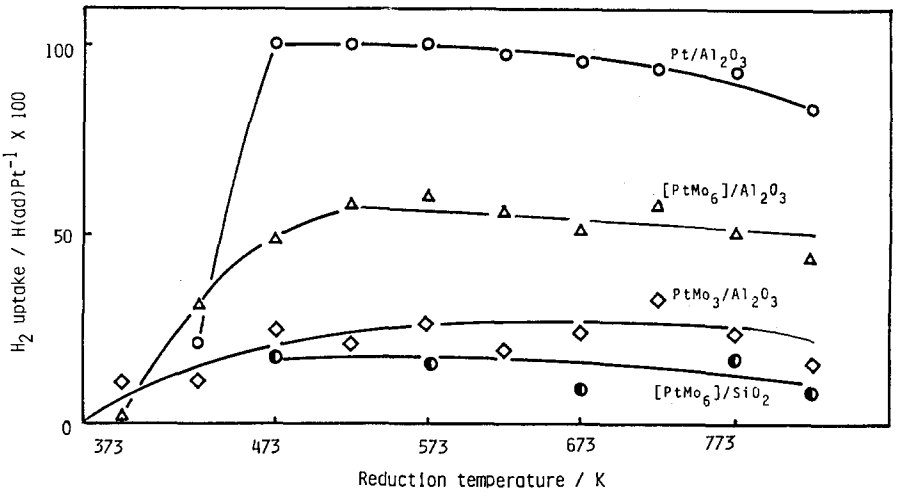

FIG. 2. H_2 uptakes of Pt/Al_2O_3, $Pt–Mo/Al_2O_3$, $[PtMo_6]/Al_2O_3$, and $[PtMo_6]/SiO_2$ reduced at various temperatures.

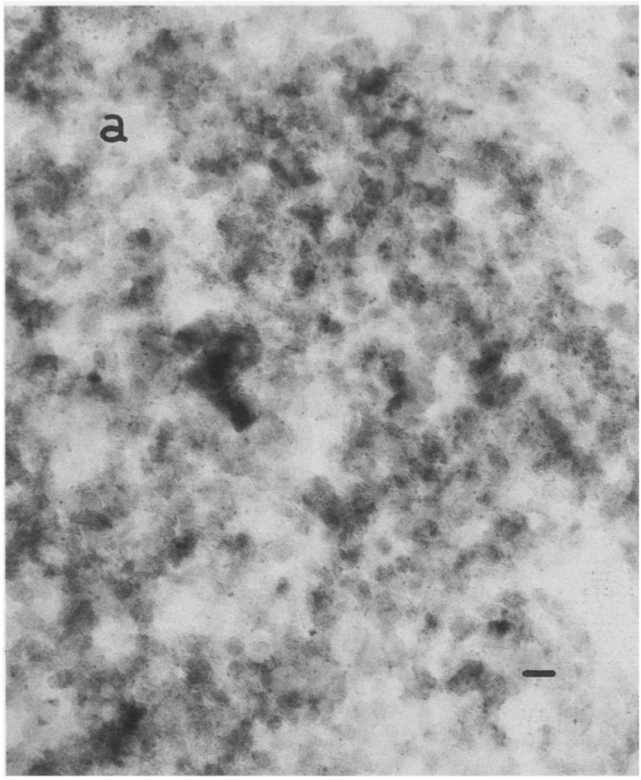

FIG. 3. Electron micrographs of various reduced catalysts: (a) $[PtMo_6]/Al_2O_3$–823R, (b) $[PtMo_6]/SiO_2$–773R, (c) $Pt–Mo/Al_2O_3$–773R (×250,000; bar denotes 20 nm).

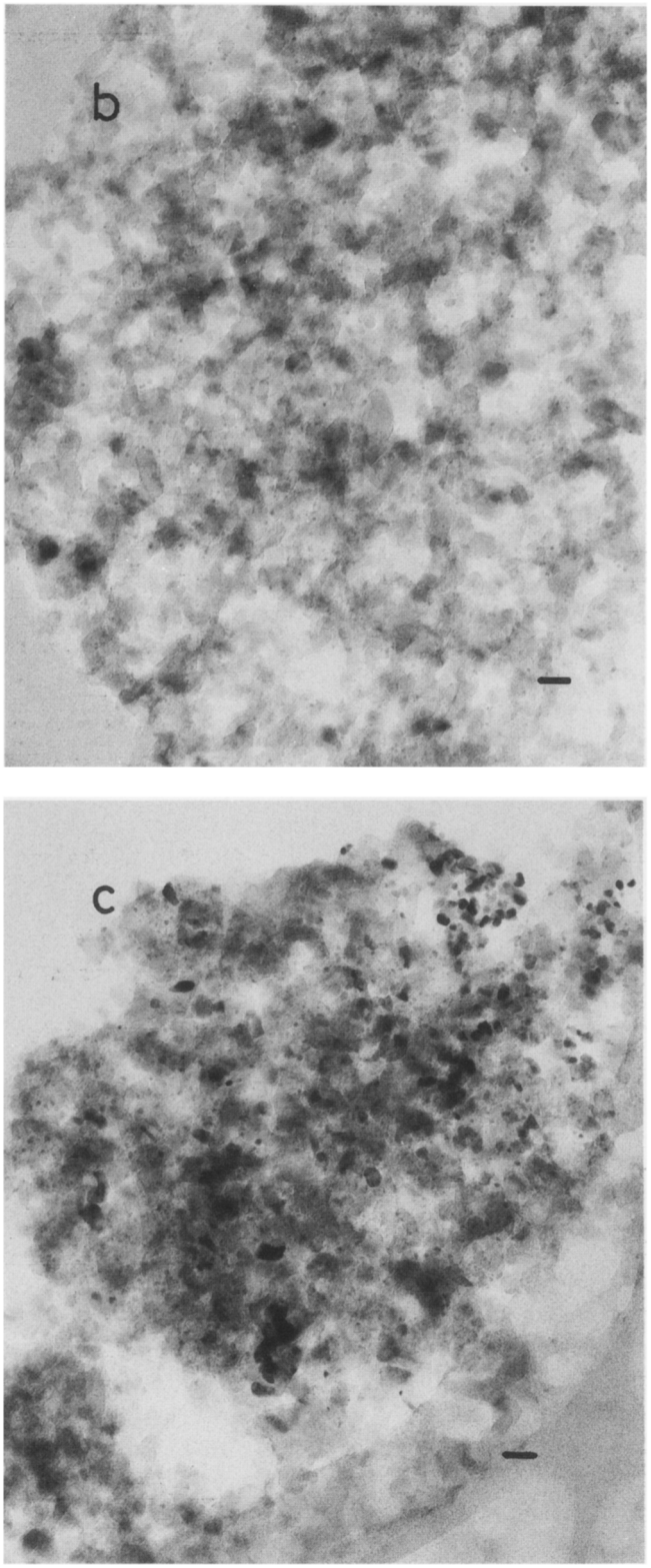

FIG. 3—*Continued*

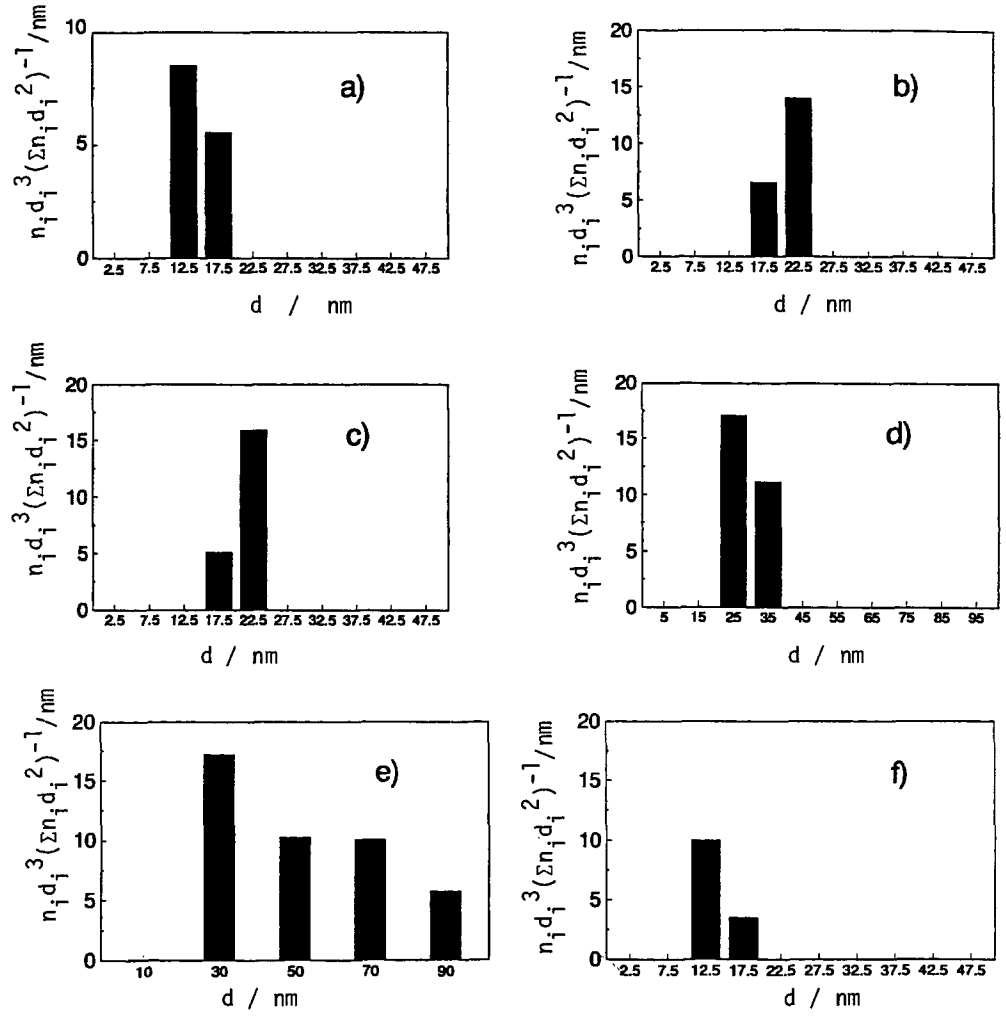

FIG. 4. Particle size distribution of various reduced catalysts: (a) $[PtMo_6]/Al_2O_3$–573R, (b) $[PtMo_6]/Al_2O_3$–773R, (c) $[PtMo_6]/Al_2O_3$–823R, (d) $[PtMo_6]/SiO_2$–773R, (e) Pt–Mo/Al_2O_3–773R, (f) Pt/Al_2O_3–773R. (d_i and n_i denote the particle size and the number of the particle, respectively.)

particle size for $[PtMo_6O_{24}]^{8-}/SiO_2$–773R is calculated to be 15 nm from H_2 adsorption assuming that only the Pt atom can adsorb H_2 and the adsorption stoichiometry of H/Pt = 1. The value is very different from the value (3.0 ± 0.5 nm) estimated by TEM, as shown in Table 1. The decrease of the H/Pt ratio with an increase of the Mo/Pt composition in bimetallic catalysts has been reported by Leclercq *et al.* (*12*) and Tri *et al.* (*3, 10*). They demonstrated that the decrease of H_2 chemisorption results from the coverage of platinum particles with molybdenum oxide. Therefore, almost 100% of the surface of Pt particles may be covered with MoO_x in $[PtMo_6]/SiO_2$–773R. For Pt/Al_2O_3 the particle sizes determined by TEM and H_2 chemisorption are almost the same.

Analytical TEM

The local chemical compositions of the particles in $[PtMo_6]/SiO_2$–773R and $[PtMo_6]/Al_2O_3$–823R catalysts were checked by the characteristic X-ray fluo-

TABLE 1

Particle Size Detected by TEM (d_{TEM}) and Average Size Calculated from Hydrogen Adsorption (d_{av})

Catalyst	Pt/Al_2O_3	$[PtMo_6]/Al_2O_3$	$Pt–Mo/Al_2O_3$	$[PtMo_6]/SiO_2$
d_{TEM}	1.5 ± 0.5	2.0 ± 0.5	2.0–20.0	3.0 ± 0.5
d_{av}	1.3	3.3	5.0	15.0

rescence from the Pt–Mo particles excited by electron microbeam. The space resolution was 10 nm, which makes it possible to analyze the average composition of a few bimetallic particles as shown, for example, by the circles in the TEM photographs of Fig. 5. Figure 6 shows the X-ray fluorescence spectra measured by the analytical TEM, where the spectrum for $[PtMo_6]/SiO_2$ is expanded in the lower scale. From the spectra, the atomic ratios of Mo to Pt are calculated to be 5.5 ± 1.5 for both bimetallic samples, suggesting the local Mo/Pt composition is almost equal to the original one even after the reduction at 773–823 K.

X-ray Diffraction

No XRD patterns are observed with the $[PtMo_6]/SiO_2$ reduced at 773 K, indicating that the Pt particles are small or amorphous. The coimpregnated $Pt–Mo/Al_2O_3$ catalyst shows a strong peak at $2\theta = 39.6°$. For the reduced $[PtMo_6]/Al_2O_3$ the Pt(111) pattern is barely observable because of the overlap of the diffraction pattern of Pt with that of γ-Al_2O_3, indicating that the Pt particle is much smaller than that in $Pt–Mo/Al_2O_3$.

EXAFS Spectroscopy

In order to examine the local structures around Pt and Mo in the bimetallic catalysts, we carried out the EXAFS analyses for the *in situ*-treated samples. The phase shift and amplitude functions for Pt–Pt, Pt–Mo, and Mo–Mo pairs were derived from the model compounds, where the designated pair, such as Pt–Mo, indicates that Pt is an absorber atom and Mo is a backscatterer atom. The k^3-weighted EXAFS oscillations and their associated Fourier transforms of the model compounds are shown in Fig. 7. The structural parameters, the Fourier transform range, and the Fourier filtering range are shown in Table 2. Two peaks appearing in the Fourier transform of $[PtMo_6O_{24}]^{8-}$, as shown in Fig. 7d, can be attributed to Pt–O (0.200 nm) and Pt–Mo (0.331 nm) bonds according to the molecular framework in Fig. 1. Since the two shells are well separated from each other, the phase shift and the amplitude functions for the Pt–Mo pair can be estimated from the EXAFS of $[PtMo_6O_{24}]^{8-}$. The Pt–Mo distances of the reference compound used and the $[PtMo_6]/Al_2O_3$–823R catalyst are 0.331 and 0.276 nm (shown later), respectively. Therefore, it is necessary to carry out the mean free path correction to obtain the accurate coordination number (C.N.) by

$$\text{C.N.} = \text{C.N.}_{\text{unc}} \times \exp(2(r_j - r_{\text{ref}})/\lambda) \fallingdotseq \text{C.N.}_{\text{unc}} \times 0.8, \quad (1)$$

where λ is assumed to be about 0.6 nm (*18*) and C.N._{unc} means uncorrected coordination number. The estimated phase shift and amplitude function for Pt–Pt, Pt–Mo, and Mo–Mo pairs are shown in Fig. 8. Backscattering amplitude $F(k)$ is calculated by

$$k^3(r^2/M)A(k) = F(k) \exp(-2\sigma^2k^2) \exp(-2r/\lambda), \quad (2)$$

where $A(k)$ is the experimentally determined amplitude and σ is assumed to be 0.006 nm. The phase shift of Mo–Pt is calculated by

$$\phi_{\text{Mo–Pt}}(k) = \phi_{\text{Pt–Pt}}(k) + \phi_{\text{Mo–Mo}}(k) - \phi_{\text{Pt–Mo}}(k). \quad (3)$$

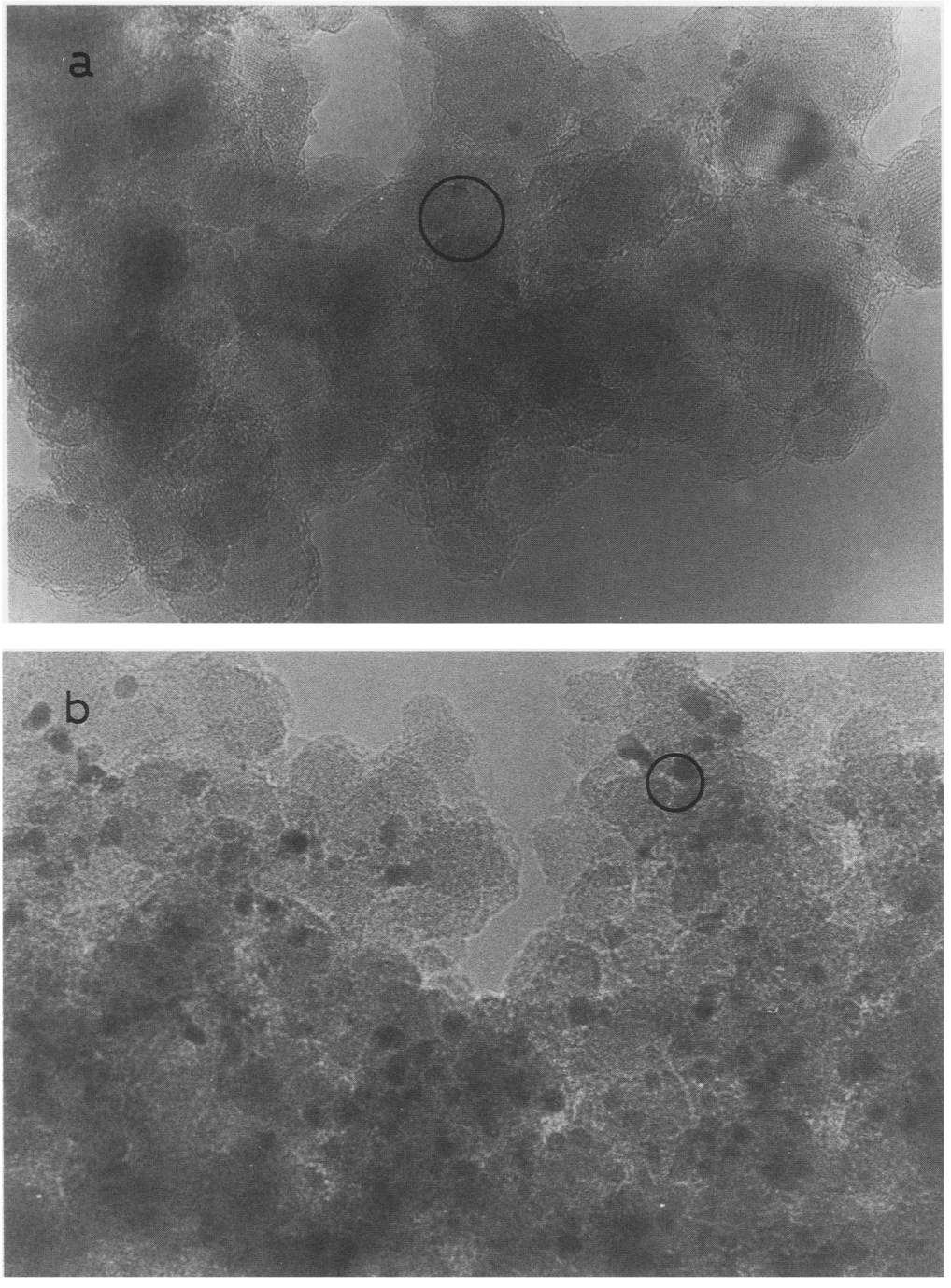

FIG. 5. Electron micrographs of (a) $[PtMo_6]/Al_2O_3$–823R (×1,500,000), (b) $[PtMo_6]/SiO_2$–773R (×1,000,000); circle, size of electron beam spot, corresponding to 10 nm.

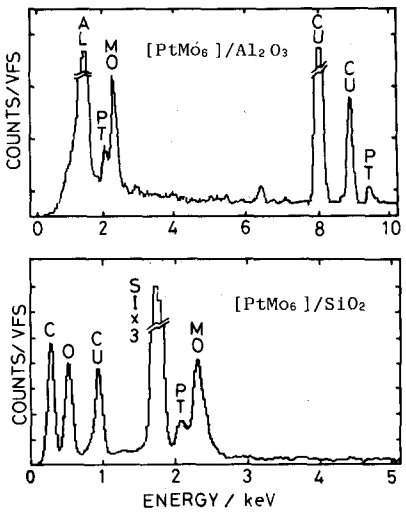

FIG. 6. Pt and Mo X-ray fluorescence emitted from catalysts irradiated by the electron beam (10 nm).

Note that the difference in the phase shifts of Pt–Pt and Pt–Mo is about π in almost the entire k range. The relationship between the phase shifts of Mo–Pt and Mo–Mo is in a similar situation, which implies that the backscattering waves from Mo and Pt interfere destructively with each other when Pt and Mo are simultaneously present around the Pt atom at a similar distance.

Figures 9a and 9b show the Fourier transforms of the Pt L_3-edge EXAFS oscillation for the incipient $[PtMo_6]/Al_2O_3$ and $[PtMo_6]/SiO_2$ samples, respectively. The Pt–Mo bond around 0.3 nm is observed with the SiO_2-supported species, indicating the retention of the $[PtMo_6]$ framework at the surface, whereas no peak for the Pt–Mo bond is observed for the Al_2O_3-supported species, suggesting the destruction of the framework after deposition onto the Al_2O_3 surface. The Mo K-edge EXAFS Fourier transform for the incipient $[PtMo_6]/SiO_2$ in Fig. 9d exhibits a peak at 0.3–0.35 nm, which arises from Mo and Pt backscattering. However, no peak around 0.3–0.35 nm is observed with the incipient $[PtMo_6]/Al_2O_3$ sample. These Mo K-edge EXAFS data coincide with the Pt L_3-edge EXAFS data. The curve-fitting results are shown in Table 3. Consequently, the $[PtMo_6]$ framework of the heteropolyanion is retained on the SiO_2 surface, but it is broken to each component without Pt–Mo and Mo–Mo bonds on the Al_2O_3 surface. The Mo species on Al_2O_3 are present in a tetrahedral symmetry like that of K_2MoO_4, judging from the Mo–O distance at 0.172 nm and the coordination number of 3.7.

Figure 10 shows the associated Fourier transforms (Figs. 10a, 10d, 10g), the EXAFS oscillations (Figs. 10b, 10c, 10h), and the curve-fitting results (Figs. 10c, 10f, 10i) for $[PtMo_6]/SiO_2$–773R, Pt–Mo/Al_2O_3–773R, and $[PtMo_6]/Al_2O_3$–823R catalysts, respectively. The curve-fitting analyses for the EXAFS data are listed in Table 4. Only Pt–Pt bonding is observed with the $[PtMo_6]/SiO_2$–773R catalyst, suggesting the formation of platinum particles. The coordination number of Pt–Pt is determined to be 4.7 as shown in Table 4. The particle size of platinum could be estimated from the coordination number to be 1.0 ($\pm$0.5 nm) on the assumption of spherical shape (*17*). The EXAFS data for the coimpregnated Pt–Mo/Al_2O_3 catalyst are similar to those for Pt foil. The Pt–Pt bond in the Pt–Mo/Al_2O_3 catalyst is observed to be 0.276 nm, which is similar to the 0.2775 nm of Pt bulk. The coordination number of Pt–Pt, 9.5, suggests Pt particles larger than the particles in $[PtMo_6]/SiO_2$, which is compatible with the TEM results. In contrast to those catalysts, the $[PtMo_6]/Al_2O_3$ catalyst showed a different feature in the EXAFS oscillation and also in its associated Fourier transform as shown in Figs. 10g and 10h. No good fitting is obtained when only the Pt–Pt bond is assumed. The best fitting result is given in Fig. 10i, where both Pt–Pt and Pt–Mo bonds are included. The present curve-fitting analysis required two-shell fitting with eight adjustable parameters. So, the curve-fitting result should be checked by other means of analysis. First we carried out the fitting analysis for k and k^2-weighted EXAFS data and found no significant difference from the data in Table 4. Then we carried out a further check by fitting the observed Fourier trans-

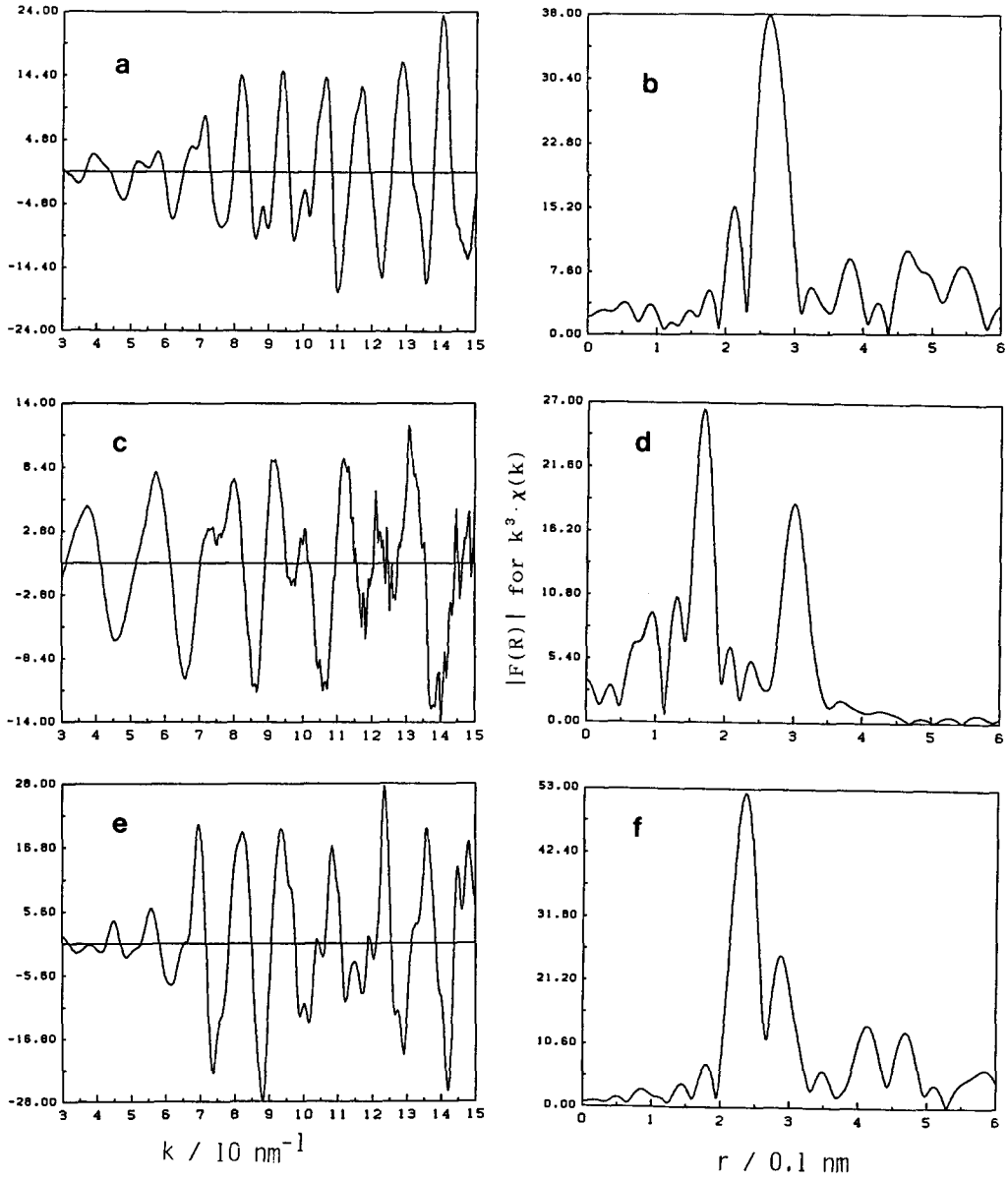

FIG. 7. k^3-weighted EXAFS and Fourier transform of Pt foil (a,b), $[PtMo_6O_{24}]^{8-}$ (c,d), Mo foil (e,f).

form with the calculated one based on the Pt–Pt and Pt–Mo model functions. Curves a and b in Fig. 11 are the k^3-weighted Fourier transforms of the Pt–Mo model functions with C.N. = 3.1, r = 0.276 nm, and σ = 0.006 nm, and the Pt–Pt model function with C.N. = 6.2, r = 0.273 nm, and σ = 0.009 nm, respectively. Summation of (a) and (b) gives (c) in Fig. 11, which resembles neither Pt–Pt nor Pt–Mo pairs but reproduces the observed Fourier transform (d) for $[PtMo_6]/Al_2O_3$–823R, exhibiting the characteristic shoulder shape, position, and amplitude. Note that the Fourier transform structures appearing at 0.2 and 0.3 nm do not arise from the real bonding at corresponding distances

TABLE 2

Lists of Parameters Used to Elucidate the Phase Shift and Amplitude Functions from Model Compounds

Compound	FT[a] range (nm^{-1})	FF[a] range (nm)	Absorber	Scatterer	C.N.	R (nm)
Pt foil	30–150	0.18–0.31	Pt	Pt	12	0.277
$[PtMo_6O_{24}]^{8-}$	30–150	0.26–0.35	Pt	Mo	6	0.331
	30–150	0.10–0.20	Pt	O	6	0.200
Mo foil	30–150	0.19–0.27	Mo	Mo	8	0.272

[a] FT, Fourier transform; FF, Fourier filtering.

but from the interference of the two shells (Pt–Pt and Pt–Mo). Thus, we can conclude the presence of the Pt–Mo bond in the $[PtMo_6]/Al_2O_3$ catalyst. The coordination numbers of Pt–Pt and Pt–Mo bonds are determined to be 6.2 and 3.1, as shown in Table 4. These results indicate the formation of Pt–Mo alloy particles on the Al_2O_3 surface. That the Debye–Waller factor (σ = 0.009 nm for the Pt–Pt bond) is larger than those for $[PtMo_6]/SiO_2$ and $Pt–Mo/Al_2O_3$ also indicates a relatively large disorder induced by the formation of Pt–Mo bonding having an atomic radius different than that of Pt.

The Mo k^2-weighted EXAFS oscillations and Fourier transforms for $[PtMo_6]/SiO_2$–773R and $[PtMo_6]/Al_2O_3$–823R are shown in Fig. 12. The $[PtMo_6]/SiO_2$ catalyst has a Mo–Mo peak at 0.24–0.30 nm, but the $[PtMo_6]/Al_2O_3$ catalyst does not. In addition to the different feature of the structures around the Pt atom between $[PtMo_6]/SiO_2$ and $[PtMo_6]/Al_2O_3$, the difference in the situation of Mo atoms between the two catalysts is also obvious. The MoO_x species are aggregated on SiO_2, while they are dispersed on Al_2O_3. The curve-fitting results for the Mo K-edge EXAFS data are shown

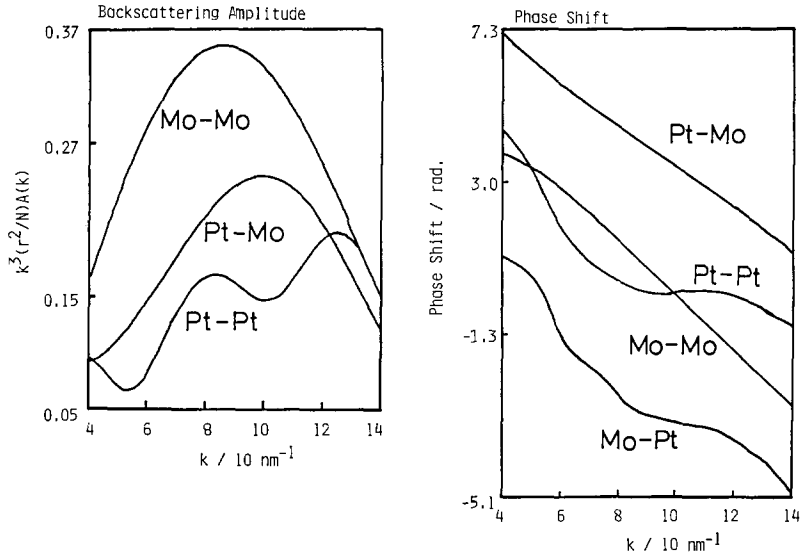

FIG. 8. Backscattering amplitude and phase shift functions of some absorbers and scatterers.

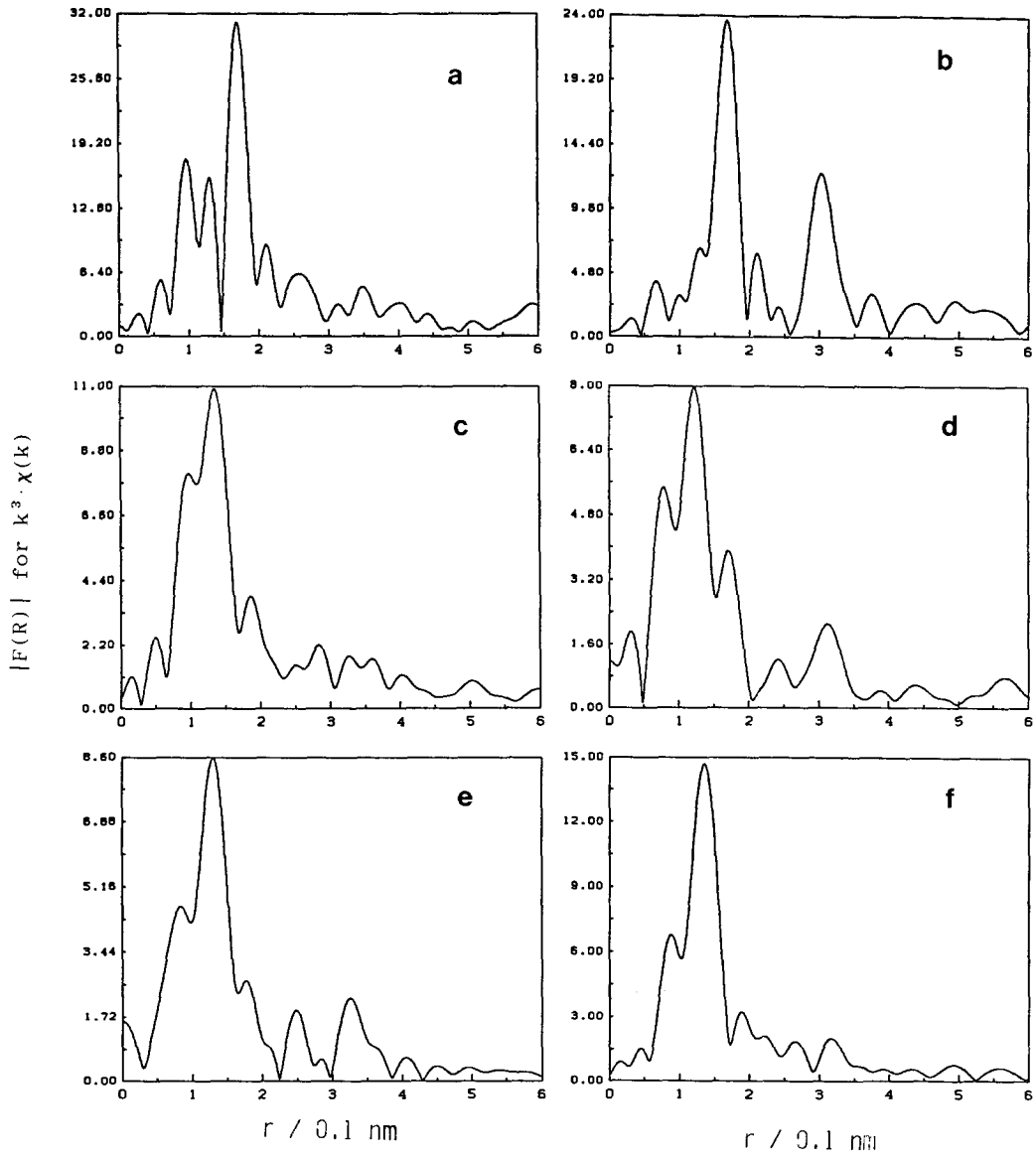

FIG. 9. The k^3-weighted Fourier transforms of incipient catalysts: (a) Pt edge of $[PtMo_6]/Al_2O_3$, (b) Pt edge of $[PtMo_6]/SiO_2$, (c) Mo edge of $[PtMo_6]/Al_2O_3$, (d) Mo edge of $[PtMo_6]/SiO_2$, (e) Mo edge of $[PtMo_6O_{24}]^{8-}$, (f) Mo edge of K_2MoO_4.

in Table 5. Irrespective of any evidence of the presence of Pt–Mo bonding in the Pt L_3-edge EXAFS analysis, the Mo–Pt contribution is not observed in $[PtMo_6]/Al_2O_3$–823R because the Mo/Pt ratio is 6 and most of the Mo atoms are located on Al_2O_3.

Figure 13 shows the Pt L_3-edge EXAFS oscillation for $[PtMo_6]/Al_2O_3$ reduced at 573–823 K. From the EXAFS analysis the platinum of $[PtMo_6]/Al_2O_3$–473R is not completely reduced, exhibiting a Pt–O bond peak in addition to a Pt–Pt peak. The platinum in $[PtMo_6]/Al_2O_3$–573R is reduced to a metallic level according to the EXAFS data and the Pt L_3- and Pt L_2-edge structures described hereinafter. The EXAFS oscilla-

TABLE 3

Curve-Fitting Results for the EXAFS Data of the Incipient $[PtMo_6]/SiO_2$ and $[PtMo_6]/Al_2O_3$ Samples

Catalyst	Model	FF (nm)	C.N.	R (nm)
$[PtMo_6]/SiO_2$	Pt–O	0.10–0.20	6.2 ± 0.4	0.199 ± 0.002
	Pt–Mo	0.26–0.35	4.2 ± 0.3	0.332 ± 0.002
	Mo–O	0.10–0.20	1.6 ± 0.2	0.165 ± 0.002
$[PtMo_6]/Al_2O_3$	Pt–O	0.10–0.20	6.0 ± 0.3	0.200 ± 0.002
	Mo–O	0.10–0.18	3.7 ± 0.4	0.172 ± 0.002

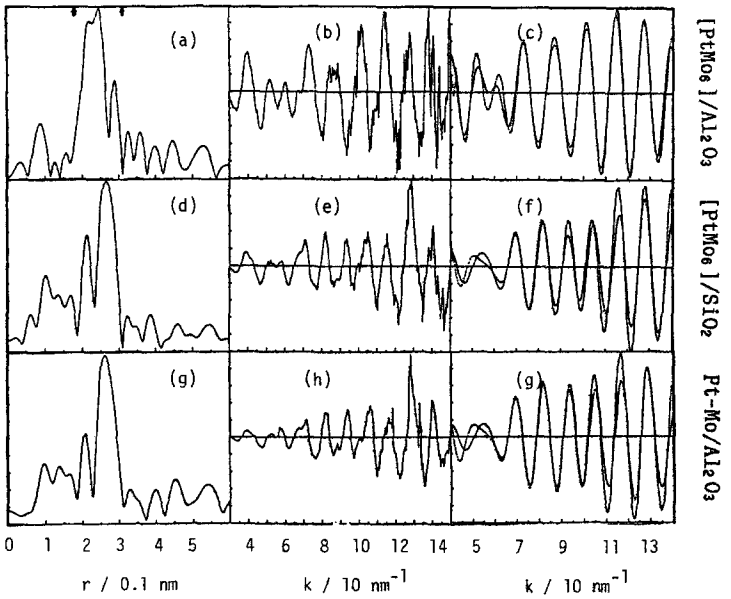

FIG. 10. Pt L_3-edge Fourier transforms, k^3-weighted EXAFS oscillations' curve fitting results of $[PtMo_6]/SiO_2$–773R (a–c), Pt/Al_2O_3–773R (d–f) and $[PtMo_6]/Al_2O_3$ –823R (g–i); dashed lines indicate the best fitting results.

TABLE 4

Curve-Fitting Results for the EXAFS Data of the Reduced Catalysts

Catalyst	Model	C.N.	R (nm)	σ (nm)
$[PtMo_6]/SiO_2$ 773R	Pt–Pt	4.7 ± 0.3	0.278 ± 0.002	0.0053 ± 0.0008
$[PtMo_6]/Al_2O_3$ 773R	Pt–Pt	9.5 ± 0.5	0.276 ± 0.002	0.0064 ± 0.0009
$[PtMo_6]/Al_2O_3$ 823R	Pt–Pt	6.2 ± 0.5	0.273 ± 0.003	0.0090 ± 0.0010
	+ Pt–Mo	3.1 ± 0.3	0.276 ± 0.003	0.0060 ± 0.0010

Note. Fourier filtering range = 0.18–0.31 nm.

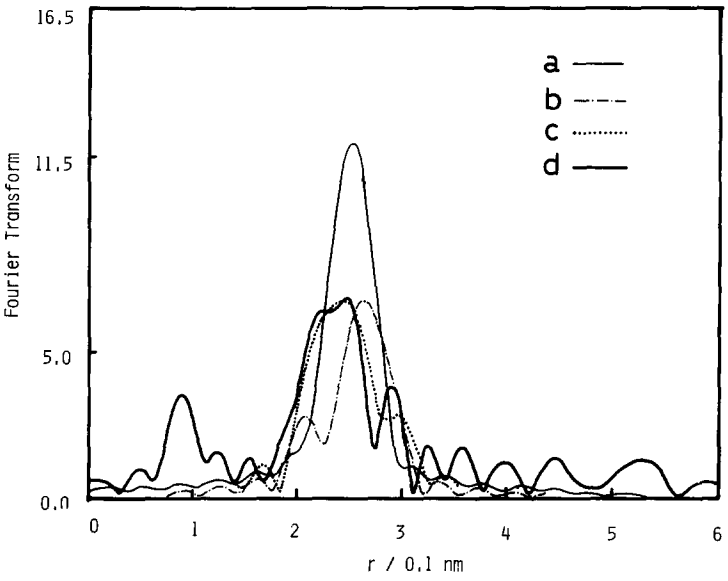

FIG. 11. The k^3-weighted Fourier transforms calculated from the model structures. (a) Pt–Mo bonding, (b) Pt–Pt bonding, (c) Pt–Mo + Pt–Pt bondings, (d) observed.

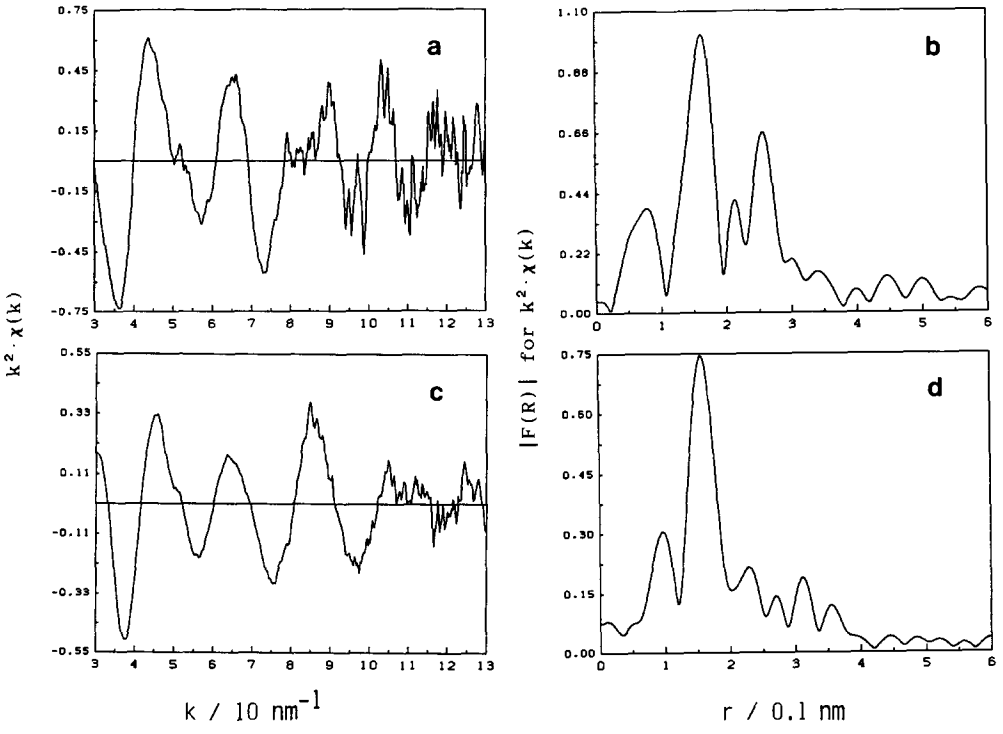

FIG. 12. k^2-weighted Mo K-edge EXAFS oscillations and their Fourier transforms of $[PtMo_6]/SiO_2$–773R (a,b) and $[PtMo_6]/Al_2O_3$–823R (c,d).

TABLE 5

Curve-Fitting Results for k^2-weighted Mo *K*-edge EXAFS Data

Catalyst	Redn.	Model	*E* (eV)	C.N.	*R* (nm)	σ (nm)
$[PtMo_6]/SiO_2$	None	Mo–O		1.6 ± 0.2	0.165 ± 0.002	0.006 ± 0.001
	773R	Mo–O		3.8 ± 0.3	0.201 ± 0.002	0.008 ± 0.001
		Mo–Mo		0.8 ± 0.2	0.282 ± 0.002	0.006 ± 0.001
	823R	Mo–O		2.2 ± 0.3	0.200 ± 0.002	0.006 ± 0.001
$[PtMo_6]/Al_2O_3$	None	Mo–O	20,012	3.7 ± 0.3	0.172 ± 0.002	0.007 ± 0.001
	373R	Mo–O	20,012	3.2 ± 0.3	0.171 ± 0.002	0.007 ± 0.001
	473R	Mo–O	20,010	2.0 ± 0.2	0.169 ± 0.002	0.007 ± 0.001
	523R	Mo–O	20,003	1.1 ± 0.3	0.169 ± 0.002	0.005 ± 0.001
		Mo–O		1.0 ± 0.3	0.201 ± 0.003	0.009 ± 0.001
	573R	Mo–O	20,003	0.7 ± 0.2	0.166 ± 0.002	0.005 ± 0.001
		Mo–O		1.6 ± 0.3	0.204 ± 0.003	0.008 ± 0.001
	823R	Mo–O	20,003	1.7 ± 0.3	0.204 ± 0.003	0.008 ± 0.001

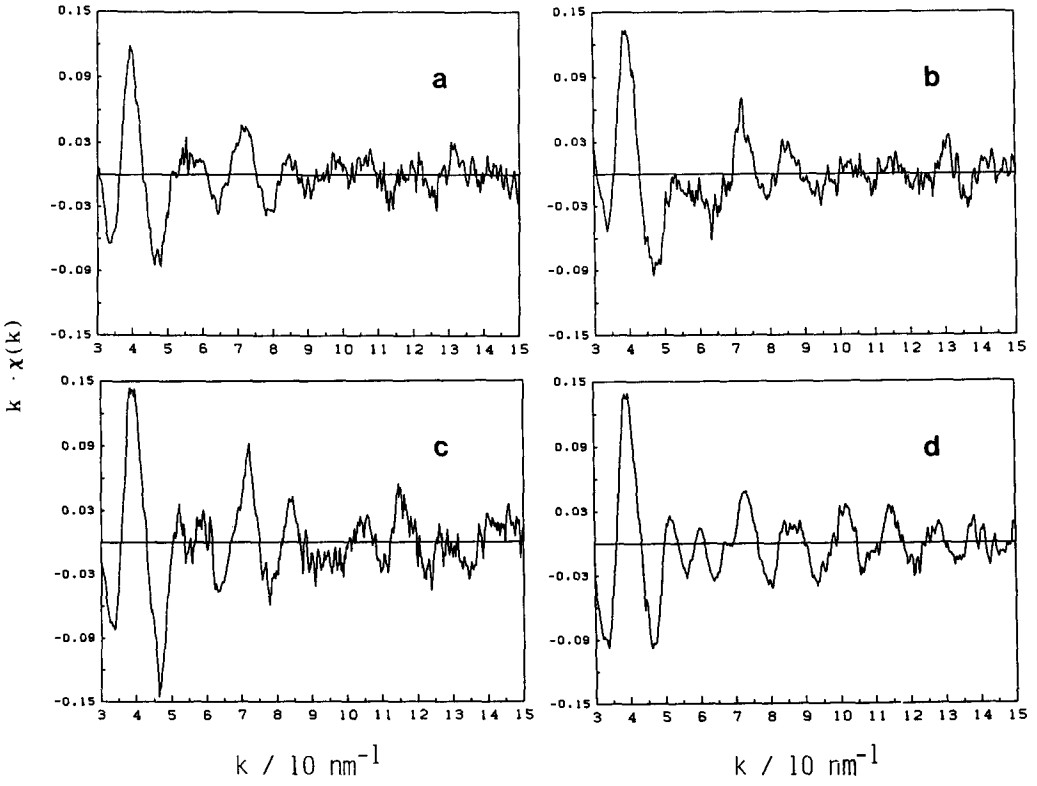

FIG. 13. *k*-weighted Pt L_3-edge EXAFS oscillations of $[PtMo_6]/Al_2O_3$ reduced at (a) 573, (b) 673, (c) 773, (d) 823 K.

tions for $[PtMo_6]/Al_2O_3$ change gradually and finally become that of $[PtMo_6]/Al_2O_3$–823R, as shown in Fig. 13. In fact, the oscillation for the sample reduced at 773 K can be reproduced by using the oscillation of $[PtMo_6]/Al_2O_3$–823R and $[PtMo_6]/Al_2O_3$–523R. Thus, the $[PtMo_6]/Al_2O_3$–573R is situated as the initial state for the formation of the Pt–Mo alloy particles. However, the EXAFS oscillation for $[PtMo_6]/Al_2O_3$–573R damps quickly. Therefore, the direct elucidation of the structure of $[PtMo_6]/Al_2O_3$–573R is rather difficult. TEM and H_2-adsorption data depicted the particle size in $[PtMo_6]/Al_2O_3$–573R as 2.0 nm, as already mentioned. Usually the Pt particles with 2.0 nm diameter exhibit the well-identified EXAFS oscillation due to Pt–Pt bonding. The exact reason for the quick damp of the EXAFS oscillation is not clear, but this feature must be related to some kind of strong Mo–Pt interaction, which may induce a large disorder in the Pt–Pt bonding.

The EXAFS data for the incipient $[PtMo_6]/SiO_2$ and $[PtMo_6]/Al_2O_3$ catalysts reveal the Mo=O double bond peak at 0.165 or 0.172 nm, respectively. The coordination number of doubly bound oxygen is gradually reduced by increasing the reduction temperature and eventually at 823 K is replaced by the Mo–O single bond at 0.201–0.204 nm as shown in Table 5. Figure 14 shows the Mo *K*-edge XANES spectra for $[PtMo_6]/Al_2O_3$. The position and shape of the Mo *K*-edge can give some information about its oxidation state. Enhancement of the $1s$–$4d$ transition often occurs in the XANES spectra of molybdenum complexes with the doubly bound oxygen, and the intensity of this transition varies with the number of Mo=O (*19*). The $1s$–$4d$ transition peak decreases in intensity to shoulder when the sample is reduced at 573 K. Our previous work on the Mo dimers attached to SiO_2 suggests that Mo has an oxidation state of less than 4+ (*20*). The shoulder then gradually diminishes with the increasing reduction temperature. The shoulder structure still appears in

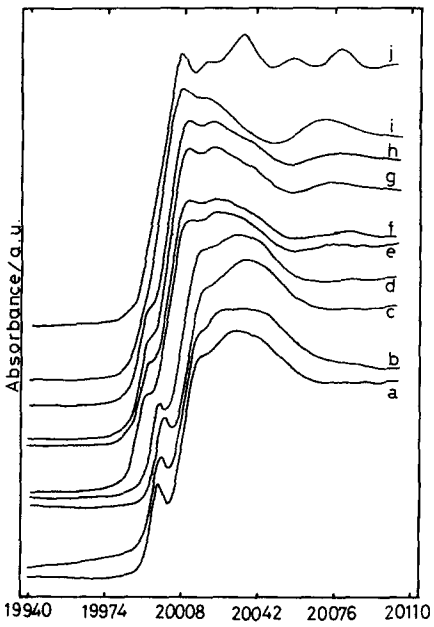

FIG. 14. Mo *K*-edge X-ray near edge structures: (a) K_2MoO_4, (b) incipient $[PtMo_6]/Al_2O_3$, $[PtMo_6]/Al_2O_3$, reduced at (c) 373, (d) 473, (e) 523, (f) 573, (g) 773, (h) 823, (i) $[PtMo_6]/SiO_2$–773K, and (j) Mo foil.

$[PtMo_6]/Al_2O_3$–823R, suggesting the presence of the double bond oxygen after the reduction at 823 K although some Mo is incorporated into Pt particles to form the Pt–Mo alloy. Since $[PtMo_6]/SiO_2$–773R showed no shoulder structure, the Mo species supported on alumina is more difficult to reduce compared to those on silica. By comparing with the Mo *K*-edge structures of Mo dimers attached to SiO_2, the Mo species in the $[PtMo_6]/SiO_2$–773R catalyst, which has no shoulder structure, is suggested to be less than 2+ (*20*).

Pt L_2- and Pt L_3-edge XANES spectra of the reduced catalysts are shown in Figs. 15 and 16. The intensities of the white lines of Pt L_2- and Pt L_3-edges increase with the reduction of samples at 773 K. The intensities of the white lines may be related to the density of the unfilled *d* state. The densities of the unfilled *d* orbital (f_d) (*21, 22*) relative to f_d for Pt foil are calculated to be 0.23, 0.21, 0.20, 0.06, and −0.06 for $[PtMo_6]/$

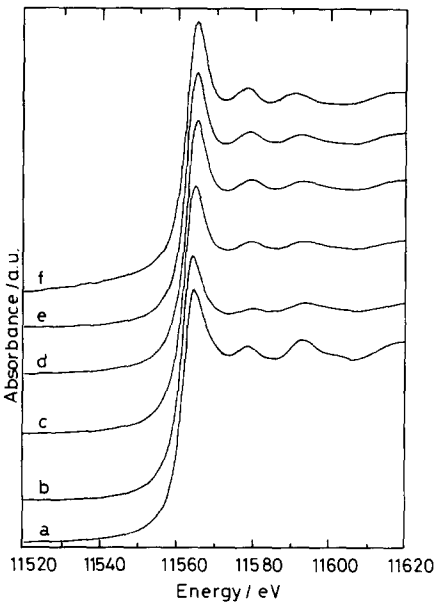

FIG. 15. Pt L_3 XANES: (a) Pt foil, (b) Pt/Al_2O_3–773R, (c) $[PtMo_6]/Al_2O_3$–573R, (d) $[PtMo_6]/Al_2O_3$–773R, (e) $[PtMo_6]/Al_2O_3$–823R, and (f) $[PtMo_6]/SiO_2$–773R.

SiO_2–773R (f), $[PtMo_6]/Al_2O_3$–823R (e), $[PtMo_6]/Al_2O_3$–773R (d), $[PtMo_6]/Al_2O_3$–573R (c), and Pt/Al_2O_3 (b) respectively, using

$$f_d = (\Delta A_3 + 1.11\Delta A_2)/(A_{3r} + 1.11A_{2r})$$
$$\Delta A_3 = A_{3s} - A_{3r}, \quad \Delta A_2 = A_{2s} - A_{2r}, \quad (4)$$

where A_{3s}, A_{3r}, A_{2s}, and A_{2r} are the white line areas of L_3- and L_2-edges of the sample and the reference, respectively. The Pt of Pt/Al_2O_3–773R shows an f_d value similar to that of Pt foil. The Pt of $[PtMo_6]/Al_2O_3$–573R is also similar to that in Pt foil with regard to d electron deficiency.

It may seem strange that the density of the unfilled state increases with the reduction temperature. This is nearly the onset of the change in the EXAFS and the formation of Pt–Mo alloy particles. A possible explanation is the electron transfer from Pt to Mo through Pt–Mo direct bonding or through $[Pt]_m/[MoO_x]_n$ interface, although the electronegativity of Pt bulk is a little larger than that of Mo bulk. But the work function/ionization potential of samples must change with the particle size/number of atoms and the situation of the samples. The L_2- and L_3-edge energies reflect the electron deficiency of Pt (*23*), but there was little difference in the edge energies for these samples within 0.3 eV. Horsely reported that the areas of L_2- and L_3-edge white lines are not always proportional to the density of the unfilled d electron state (*24*). The behavior of the f_d change cannot be completely explained at present, but we propose that the platinum bonding with molybdenum in the Pt–Mo alloy particles may be somewhat electronically deficient.

Structure Models

The structure models for $[PtMo_6]$ particles on SiO_2 and Al_2O_3 based on H_2 adsorption, TEM image, analytical TEM, EXAFS, and XANES are illustrated in Fig. 17. When the plane $[PtMo_6O_{24}]^{8-}$ is supported on silica, the framework of the heteropolyanion is retained. After the reduction at 773 K the "eggshell" particles of 3.0 nm, in which the

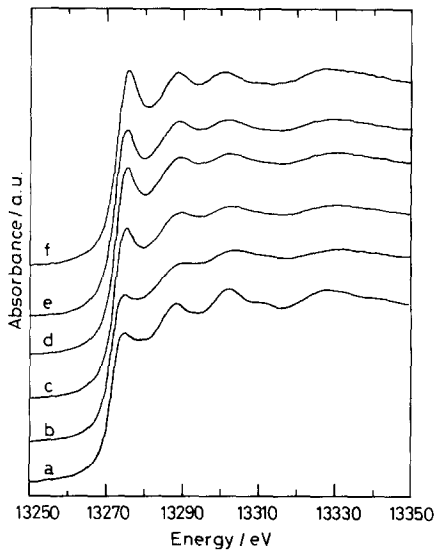

FIG. 16. Pt L_2 XANES: (a) Pt foil, (b) Pt/Al_2O_3–773R, (c) $[PtMo_6]/Al_2O_3$–573R, (d) $[PtMo_6]/Al_2O_3$–773R, (e) $[PtMo_6]/Al_2O_3$–823R, and (f) $[PtMo_6]/SiO_2$–773R.

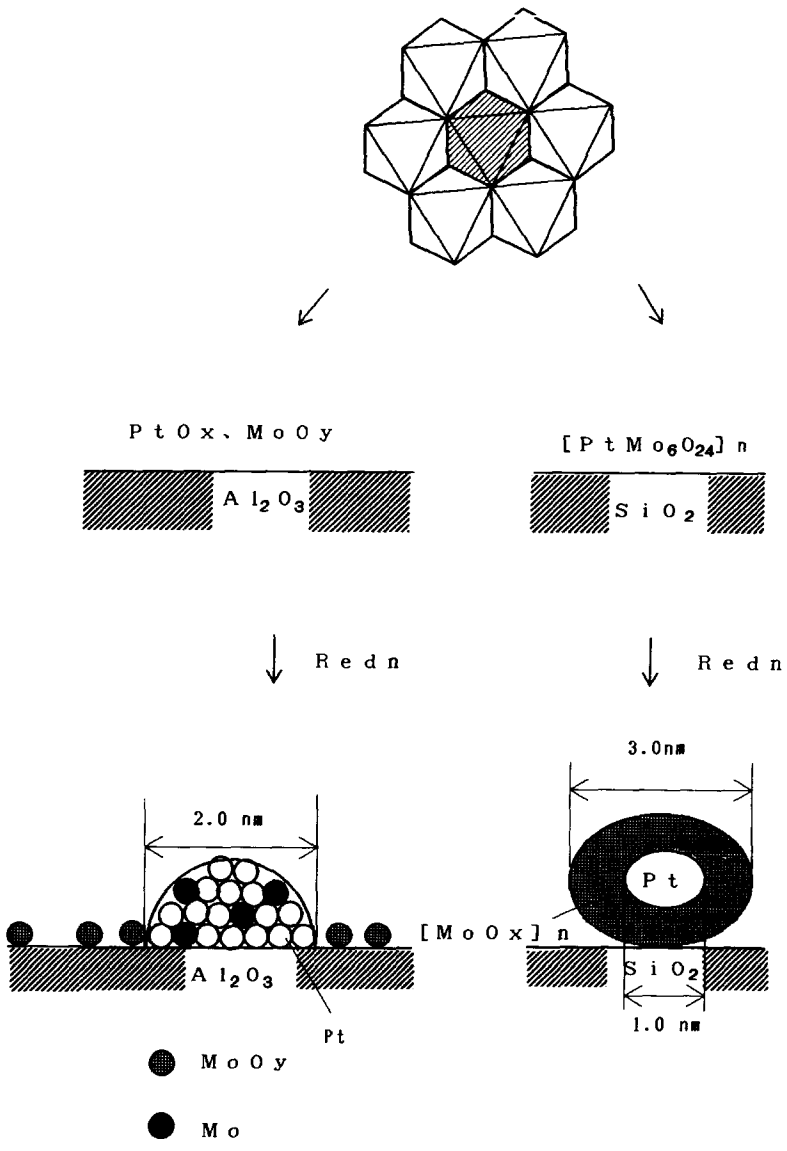

FIG. 17. Structure models for the reduced $[PtMo_6]/Al_2O_3$ and $[PtMo_6]/SiO_2$ catalysts.

platinum particle core of about 1.0 nm is surrounded by the Mo(II)-oxide layer, are formed. In the case of the alumina-supported catalyst the polyanion structure is broken upon interaction with alumina. After the reduction at 823 K, the bimetallic Pt–Mo particles of 2.0 nm are formed. The platinum atoms bonding with molybdenum atoms at a distance of 0.276 nm in the bimetallic particles are electronically deficient compared with those of Pt foil. The rest of the partially reduced molybdates may be located on the Al_2O_3 surface. The Pt–Mo alloy particles are efficiently formed from the $[PtMo_6O_{24}]^{8-}$ ensemble. The coimpregnated Pt–Mo/Al_2O_3 catalyst showed no Pt–Mo bonding. As a result, Pt aggregated into monometallic particles without any significant interaction between Mo and Pt.

In the present report the two types of

Pt–Mo bimetallic particles on SiO_2 and Al_2O_3 are formed by using the new $[PtMo_6O_{24}]^{8-}$ heteropolyanion as a precursor. That is, the eggshell structure is composed of the 1.0-nm Pt particle core and the partially reduced $Mo(2+)O_x$ shell on the SiO_2 surface with the alloy particle exhibiting a direct Pt–Mo bond at 0.276 nm on the Al_2O_3 surface. The Pt–Mo bimetallic particles of 2.0 nm on Al_2O_3 are active for ethene hydrogenation and ethane hydrogenolysis. Differences in the interaction of SiO_2 and Al_2O_3 with Pt and Mo ions determine the structure of bimetallic particles on these supports. We will discuss the catalytic performance of Pt–Mo bimetallic catalysts in part II of this report.

ACKNOWLEDGMENT

The EXAFS measurement was carried out under the approval of the Photon Factory Advisory Committee (Proposal 90-004).

REFERENCES

1. Gates, B. C., Guczi, L., and Knozinger, H., Eds., "Metal Clusters in Catalysis," Elsevier, Amsterdam/New York, 1986.
2. Asakura, K., and Iwasawa, Y., *J. Chem. Soc. Faraday Trans. 1* **84,** 2445 (1988); Asakura, K., Yamada, M., and Iwasawa, Y., *J. Chem. Soc. Faraday Trans. 1* **84,** 2457 (1988).
3. Tri, T. M., Massardier, J., Gallezot, P., and Imelik, B., *J. Catal.* **85,** 244 (1984).
4. Kuznetsov, B. N., Yermakov, Yu. I., Boudart, M., and Collman, J. P., *J. Mol. Catal.* **4,** 49 (1978).
5. Guo, X., Yang, Y., Den, M., Li, H., and Lin, A. Z., *J. Catal.* **99,** 218 (1986).
6. Yermakov, Yu. I., and Kuznetsov, B. N., *J. Mol. Catal.* **9,** 13 (1980).
7. Shulga, Yu. M., Moravskaya, T. M., Kuznetsov, B. N., Startsev, A. N., Ryndin, Yu. A., Yermakov, Yu. I., and Borodko, Yu. G., *Kinet. Katal.* **20,** 1272 (1979).
8. Zaikovskii, V. I., Ryndin, Yu. A., Kovalchukl, V. I., Plyasova, L. M., Kuznetsov, B. N., and Yermakov, Yu. I., *Kinet. Katal.* **22,** 443 (1981).
9. Yermakov, Yu, Kuznetsov, B. N., and Rydin, Yu. A., *J. Catal.* **42,** 73 (1976).
10. Tri, T. M., Candy, J. P., Gallezot, P., Massardier, J., Primet, M., Vedrine, J. C., and Imelik, B., *J. Catal.* **79,** 396 (1983).
11. Samant, G. M., Bergeret, G., Meitzner, G., Gallezot, P., and Boudart, M., *J. Phys. Chem.* **92,** 3547 (1988).
12. Leclercq, G., Romero, T., Pietrzyk, S., Grimblot, J., and Leclercq, L., *J. Mol. Catal.* **25,** 67 (1984).
13. Lee, U., Ph.D. thesis, University of Tokyo, 1984.
14. Liu, T., Matsui, Y., Asakura, K., Lee, U., and Iwasawa, Y., "Proceedings, 1st Tokyo Conference on Advanced Catalytic Science and Technology," Kodansha, Tokyo (1991), p. 267.
15. Oyanagi, H., Matsushita, T., Ito, M., and Kuroda, H., *KEK Rep.* No. 83 (1984); Nomura, M., *KEK Rep.* No. 85 (1985).
16. Kosugi, N., and Kuroda, H., "Program EXAFS 2." University of Tokyo (1987).
17. Greegor, R. B., and Lytle, F. W., *J. Catal.* **63,** 476 (1980).
18. Stern, E. A., Bunker, B. A., and Heald, S. M., *Phys. Rev. B* **21,** 5521 (1980).
19. Cramer, S. P., Hodgson, K. O., Gillum, W. O., and Mortenson, L. E., *J. Am. Chem. Soc.* **100,** 3398 (1978).
20. Kuroda, H., Kosugi, N., Ishii, H., Asakura, K., Yokoyama, T., and Iwasawa, Y., "PF Activity Report," Vol. 1, No. IV, p. 54, 1983.
21. Mansour, A. N., Cook, J. W., Sayers, D. E., Emrich, R. J., and Katzer, J. R., *J. Catal.* **89,** 462 (1984).
22. Yoshitake, H., and Iwasawa, Y., *J. Phys. Chem.* **95,** 7368 (1991); *J. Catal.* **131,** 276 (1991).
23. Hilbrig, F., Michel, C., and Haller, G. L., in press.
24. Horsley, J. A., *J. Chem. Phys.* **76,** 1451 (1982).